ARTICLE   OPEN

Check for updates

Tunable sliding ferroelectricity and magnetoelectric coupling in two-dimensional multiferroic MnSe materials

Kehan Liu[1], Xikui Ma[1], Shuoke Xu[1], Yangyang Li[1] and Mingwen Zhao[1 ✉]

Sliding ferroelectricity (SFE) found in two-dimensional (2D) van der Waals (vdW) materials, such as BN and transition-metal dichalcogenides bilayers, opens an avenue for 2D ferroelectric materials. Multiferroic coupling in 2D SFE materials brings us an alternative concept for spintronic memory devices. In this study, using first-principles calculations, we demonstrate that MnSe multilayers constructed by the recently-synthesized MnSe monolayer have large sliding-driven reversible out-of-plane electric polarization ($\sim$10.6 pC m^{-1}) and moderate interlayer sliding barriers superior to the existing 2D SFE materials. Interestingly, the intrinsic electric polarization is accompanied by nonzero net magnetic moments which are also switchable via lateral interlayer sliding. Additionally, both SFE and magnetoelectric coupling can be effectively regulated by external strain and/or hole doping. Our findings suggest the potential of MnSe multilayers in 2D multiferroic and spintronic applications.

INTRODUCTION

Ferroelectric materials have switchable bistable states with opposite spontaneous electric polarization that can be reversed via external electric field, enabling application in non-volatile memory devices[1]. The traditional ferroelectric materials, such as perovskite oxide PbTiO$_3$[2], BaTiO$_3$[3], and BiFeO$_3$[4,5] where the electric polarization originates from the displacement of octahedral center ions are facing many challenging in miniaturization and integration of nanoelectronics device, mainly due to interface distortion and depolarization field[6,7]. The emergency of two-dimensional (2D) van der Waals (vdW) ferroelectric materials with atomic thickness and clean interface, such as IV–VI group compounds[8–10], CuInP$_2$S$_6$[11,12], and In$_2$Se$_3$[13,14] extends the border of ferroelectricity to few atomic layers. However, the 2D ferroelectric materials which have been achieved in experiments under ambient conditions remain rare due to stringent constrains on lattice symmetry and stability.

Sliding ferroelectricity (SFE) found in 2D vdW bilayers[15] where the out-of-plane electric polarization can be switched by lateral sliding between the two monolayers opens a fascinating avenue for 2D ferroelectricity. To date, room-temperature SFE has been observed in hexagonal boron nitride (BN)[16–18] and transition-metal dichalcogenides (TMDs)[15,19–24]. However, the electric polarization of these SFE materials is much weaker than that of the traditional ferroelectric materials. For example, the electric polarization of MoS$_2$ and WTe$_2$ are only 0.97 pC m^{-1}[25] and 0.38 pC m^{-1}[26,27], respectively. 2D SFE materials with improved electric polarization are quite crucial for the relevant functional device applications.

Additionally, the coupling of different ferroic orders (such as ferroelectricity, ferromagnetism and ferroelasticity) in multiferroic materials is essential for information processing and memory devices[28]. In particular, magnetoelectric coupling[29–31] through which magnetism can be regulated by electric field is promising for electric-writing and magnetic-reading devices. The emergency of SFE in 2D vdW materials brought us a fascinating mechanism of magnetoelectric coupling that differs significantly from the conventional multiferroics[30,32–34]. For example, the multiferroic bilayer VS$_2$ consisting of two ferromagnetic (FM) monolayers was

predicted to have electric control of magnetism via interlayer sliding based on first-principles calculations[34]. However, the layered VS$_2$ materials have not yet been synthesized in experiments. Compared to ferromagnets, antiferromagnetic (AFM) materials have the advantages of faster spin dynamics and low sensitivity to stray magnetic fields, and thus are more suitable for spintronic memory devices[35]. Therefore, searching for a 2D AFM materials with remarkable SFE and magnetoelectric coupling is of great significance for achieving SFE-controlled electron spin polarization and relevant device applications.

In this study, by means of first-principles calculations we demonstrate the enhanced SFE and magnetoelectric coupling in the antiferromagnetic 2D vdW bilayer and multilayers composed of the recently-synthesized MnSe monolayer[36]. Our computations show that MnSe bilayer has stronger electric polarization than BN and other vdW SFE bilayers accompanied by remarkable magnetoelectric coupling. The electric polarization of MnSe multilayers is stronger than that of MoS$_2$ and WTe$_2$ by more than one order. Moreover, the electric polarization and magnetism can be significantly regulated by applying external strain and/or hole doping. The tunable ferroelectricity and magnetoelectric coupling of the 2D vdW MnSe materials offer a promising platform for study of sliding multiferroics and relevant spintronics device applications.

RESULTS

Lattice structure and antiferromagnetism of MnSe monolayer

MnSe monolayer is composed of two buckled honeycomb MnSe sublayers which are linked together by Mn–Se bonds[36], as shown in Fig. 1a. The Mn/Se atoms of the upper sublayer reside alternatively atop the Se/Mn atoms of the lower sublayer. Each unit cell contains two Mn atoms and two Se atoms with the lattice constant of 4.28 Å, which belongs to the space group of P-3m1. The lengths of the in-plane and out-of-plane Mn-Se bonds in MnSe monolayer are respectively 2.58 and 2.59 Å. The height of the bucked MnSe sublayer determined from the out-of-plane distance between Mn and Se atoms is about 0.73 Å. Although each buckled MnSe sublayer has out-of-plane electric polarization,

---

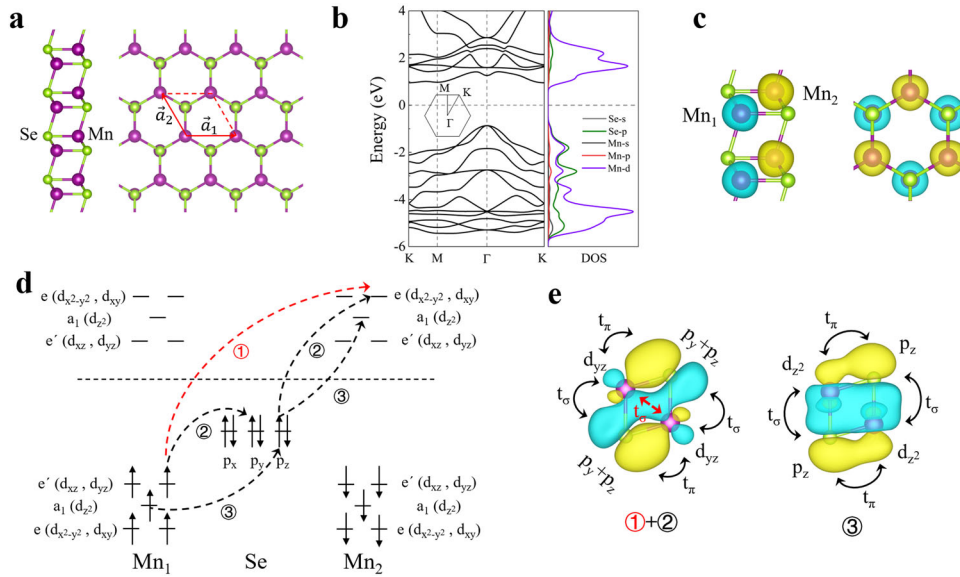[1]School of Physics, Shandong University, Jinan, China. ✉email: zmw@sdu.edu.cn

Fig. 1 Atomic configuration and electronic structures of MnSe monolayer. a Top and side views of MnSe monolayer, in which the unit cell is marked by the red arrows and dashed lines. Violet/green balls represent Mn/Se atoms. **b** Electronic band structure and projected density of states of MnSe monolayer. **c** Spin density of MnSe monolayer. The yellow/blue isosurfaces indicate spin up/down electrons. **d** Schematic diagram of the intralayer first nearest-neighbor exchange interaction in MnSe monolayer. The red/black dashed arrows represent the electron hopping paths for direct/super-exchange interactions. **e** Maximally localized Wannier functions relevant to the intralayer exchange interactions. The orbitals hybridization is denoted by the arrows.

the two MnSe sublayers in the centrosymmetric MnSe monolayer have opposite buckling, whose electric polarization cancel each other out. This feature enables us to recover the electric polarization of MnSe bilayer by breaking the equivalence of the two MnSe sublayers.

We start from the different magnetic configurations of MnSe monolayer, as depicted in Supplementary Fig. 1. Our DFT calculations show that the Neel-type AFM configuration is energetically most favorable among these magnetic configurations, which is more stable than the FM state by about 0.4 eV per unit cell, in good consistence with the previous work[36]. The robust Neel-type AFM state of MnSe monolayer contains two FM MnSe sublayers which are coupled antiferromagnetically, as depicted in Fig. 1c. The magnetic anisotropy energy (MAE) calculations involving spin-orbit coupling (SOC) effect indicate that MnSe monolayer favors isotropic in-plane magnetization rather than out-of-plane magnetization by about 0.73 meV, as shown in Supplementary Fig. 2. Moreover, it is found that SOC effect has negligible impact on the electronic band structure of MnSe monolayer, as shown in Supplementary Fig. 3.

The electronic band structures and orbital-resolved electron density of states of MnSe monolayer are depicted in Fig. 1b. Obviously, MnSe monolayer is a semiconductor with a global indirect band gap (Γ-K) of 1.72 eV and a direct band gap (Γ-Γ) of 2.05 eV. The valence band maximum (VBM) is contributed by the 3p orbitals of Se and 3d orbitals of Mn, while the conduction band minimum (CBM) arise from the 3d orbitals of Mn. Importantly, the expanded occupied states near Fermi level stem mainly from the hybridization of Se 3p orbitals and Mn 3d orbitals, which contribute to the high SFE and magnetoelectric coupling of MnSe bilayer as discussed in the following sections, the relevant orbital-resolved projected band structures are presented in Supplementary Fig. 4.

To illustrate the magnetic properties of MnSe monolayer, we consider the Heisenberg Hamiltonian:

$$H = -\sum_{i,j} J_{ij} \mathbf{s}_i \cdot \mathbf{s}_j, \qquad (1)$$

where J_{ij} are isotropic magnetic exchange parameters between spin sites i and j. The normalized $\mathbf{s}_i$ and $\mathbf{s}_j$ denote the unit vectors

Table 1. The calculated intralayer exchange parameters (in meV) of MnSe monolayer via energy mapping and MFT methods.

	J_1	J_2	J_3
Energy mapping	−32.2	−7.1	−1.0
MFT	−40.2	−9.7	−0.1

of the magnetic moment in sites i and j. FM (AFM) coupling between i and j is favored when $J_{ij} > 0$ ($J_{ij} < 0$). We extract the exchange parameters of J_1, J_2 and J_3 corresponding to intralayer exchange of first nearest-neighbor (1NN), second nearest-neighbor (2NN) and third nearest-neighbor (3NN) via mapping the DFT calculated energies of different magnetic configurations to the Heisenberg Hamiltonian, as listed in Table 1. Notably, all the exchange parameters are negative, suggesting that AFM is favored. $|J_1|$ is about five times larger than $|J_2|$ and two orders of magnitude larger than $|J_3|$. Therefore, it is the AFM exchange interaction between the 1NN sites that dominates the stable intralayer Neel-type AFM magnetic configuration of MnSe monolayer.

The magnetic exchange parameters can also be obtained using the Green's function method based on magnetic force theory (MFT), in which the total energy variation is treated as perturbation induced by spin rotations from magnetic ground state. The exchange parameters obtained from the MFT are consistent with those of the total-energy mapping method, as listed in Table 1. Furthermore, the orbital-resolved magnetic exchange parameters in the MFT allow us to reveal the microscopic magnetic exchange mechanism of MnSe monolayer. In MnSe monolayer, the 3d orbitals of Mn split into one singlet state a_1 (d_{z^2}) and two doublet states e' (d_{xz}, d_{yz}) and e ($d_{x^2-y^2}$, d_{xy}) under a crystal field with a C_{3v} symmetry. In this case, the d^5 electronic configuration of Mn^{2+} favors half-filled 3d orbital states due to on-site Coulomb interaction, giving rise to local magnetic moments of $5\mu_B$[37]. The diagram for the exchange mechanism of the local magnetic moments is depicted in Fig. 1d. The magnetic coupling highly depends on the virtual hopplings between the states of the spin
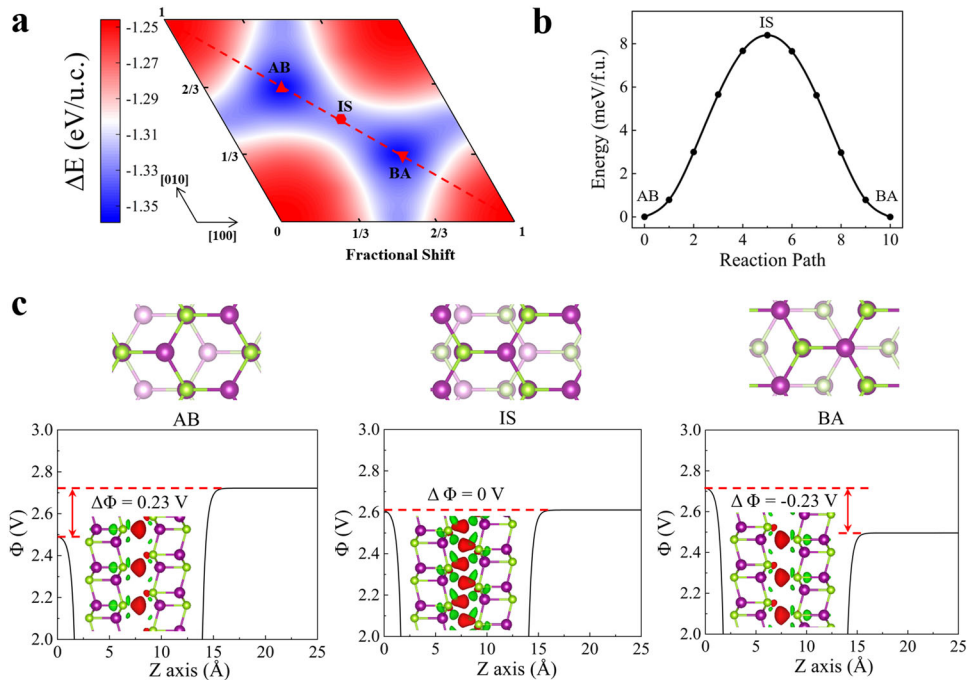
Fig. 2 Ferroelectric switching of MnSe bilayer via interlayer sliding. a The interlayer binding energy profile as a function of interlayer sliding of MnSe bilayer. **b** Ferroelectric switching pathway of MnSe bilayer. **c** Top views and plane averaged electric potential of AB, IS and BA stacking patterns of MnSe bilayer. The isosurfaces of the differential charge density of MnSe bilayer with respect to the isolated MnSe monolayers are depicted in the insets of this figure. The red and green isosurfaces respectively indicate electron accumulation and depletion.

sites which are closely related to the intralayer orbital hybridization along the hopping paths. From the orbital-resolved 1NN exchange parameter (J_1) shown in Supplementary Table 1, one can find that the magnetic exchange interaction comes mainly from a_1-a_1 and e'-e' hoppings, whereas the contributions of other hoppings are relative weak due to the constrains of symmetry. As shown in Fig. 1d, the a_1-a_1 hopping is mainly contributed by d_{z^2}-p_z-d_{z^2} hybridization which generates AFM superexchange interaction, while the e'-e' hopping arising from e'-e' and e'-p_y-p_z-e' hybridization leads to AFM direct exchange interaction and superexchange interaction, respectively. For clarity, the calculated maximally localized Wannier functions (MLWFs) relevant to the above hybridization paths are shown in the Fig. 1e, in which the Se p_z plays an important role.

Sliding ferroelectricity in MnSe bilayer

The inversion symmetry of the MnSe monolayer can be lifted by constructing a MnSe bilayer. We scan the stacking energy profile of a MnSe bilayer as upper monolayer sliding with respect to the down monolayer. Our calculations show that the stacking energy profile is irrelevant to the intralayer or interlayer magnetic configuration of MnSe bilayer, as depicted in Supplementary Fig. 5. Therefore, we focus on the MnSe bilayer with identical intralayer AFM coupling in the following computations. Two energy minimal stacking patterns (denoted as AB and BA) are found in the stacking energy profile which are energetically degenerate, as shown in Fig. 2a. They are linked by an intermediate state (IS) locating in the middle of the sliding pathway. The double-wall potential profile hints the ferroelectricity of the MnSe bilayer. In terms of AB stacking pattern, the Mn atoms of the upper monolayer are right above the Se atoms of the down monolayer, while the Mn atoms of the down monolayer are right below the center of the buckled hexagon of the upper monolayer, as marked in Fig. 2c. The interlayer distance along the out-of-plane direction between the two MnSe monolayers is 3.61 Å, suggesting the weak van der Waals interaction between them. Such interlayer inequivalence lifts the inversion symmetry and reduces

the space group to p3m1. The electron redistribution due to the interlayer inequivalence leads to charge transfer between the two monolayers and thus out-of-plane electric polarization. The intrinsic electric polarization of the MnSe bilayer is further verified by the electrostatic potential difference (~ 0.23 V) between the two monolayers, as shown in Fig. 2c, which is an order of magnitude larger than transition metal dichalcogenides (TMDs)[38]. Similar results are also found in the BA-stacked MnSe bilayer, except the opposite charge transfer and electric polarization direction. Therefore, the electric polarization direction of the MnSe bilayer can be reversed by switching the stacking pattern between AB and BA via interlayer sliding, demonstrating the SFE characteristics of MnSe bilayer.

We further explore the possible ferroelectric switching path of MnSe bilayer through the nudge-elastic-band (NEB) method, as displayed in Fig. 2b. The energy barrier of interlayer sliding between AB and BA stacking is estimated to be 8.4 meV per formula, which is much lower than those of $BiFeO_3$ (~430 meV per formula)[4] and In_2Se_3 (~ 60 meV per formula)[39] and comparable to that of BN (~4 meV per formula)[25], verifying the feasibility of ferroelectric switching and the stability of SFE of MnSe bilayer. Furthermore, as shown in Fig. 4a, the out-of-plane ferroelectric polarization of MnSe bilayer can reach 2.7 pC m^{-1}, which is larger than BN (~2.08 pC m^{-1})[25] and WTe$_2$ (~0.38 pC^{-1})[26]. Such high out-of-plane electric polarization can be ascribed to the direct electron transfer from Mn to Se ions at the interface of MnSe bilayer induced by the strong interlayer hybridization between Mn-d_{z^2} and Se-p_z, as shown in Fig. 3c. This differs significantly from the weak electric polarization of TMDs which originates from the inequivalent distribution of electrons in the interfacial chalcogens[16,24]. The enhanced electric polarization and moderate ferroelectric switching barrier manifest the high SFE of MnSe bilayer.

Magnetoelectric coupling in antiferromagnetic MnSe multilayers

The exchange interactions of the two antiferromagnetic MnSe monolayers favors AFM coupling at the interface of MnSe bilayer,
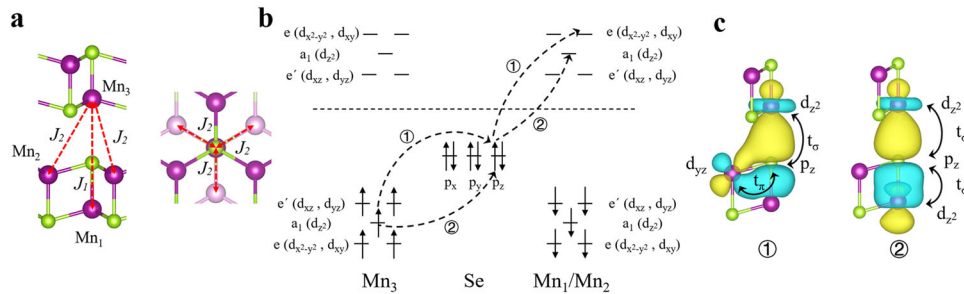
Fig. 3 Microscopic mechanism of interface AFM coupling in ferroelectric MnSe bilayer. a Top and side views of AB-stacked MnSe bilayer. The red dashed arrows indicate the interlayer exchange interactions. **b** Schematic diagram of the interlayer exchange interactions, in which the black dashed arrows denote the electron hopping paths for the interlayer super-exchange interactions. **c** Maximally localized Wannier functions relevant to the interlayer exchange interactions. The arrows indicate the orbitals hybridization.
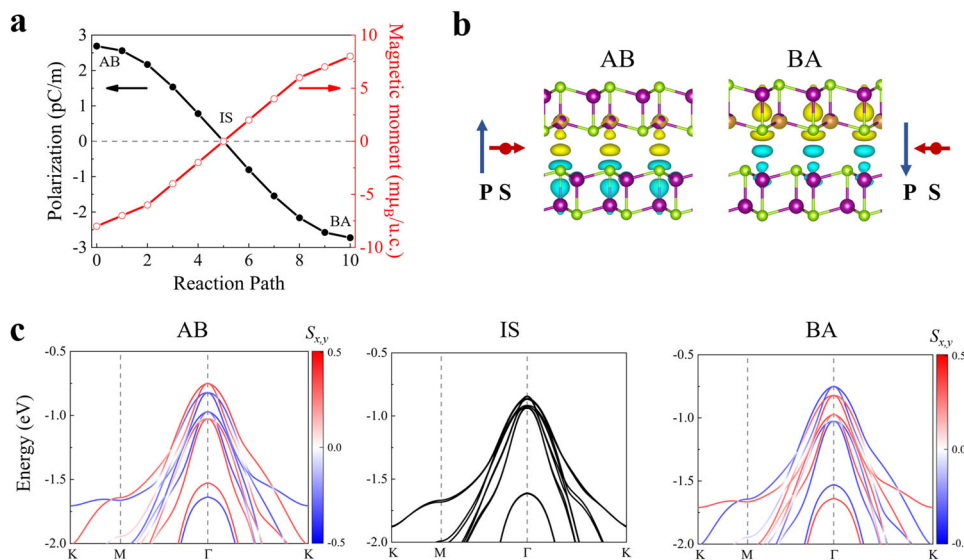

Fig. 4 Magnetoelectric coupling accompanied with electric polarization switching in MnSe bilayer. a Electric polarization and net magnetic moment variation as the interlayer sliding between AB and BA stacking in MnSe bilayer. **b** Differential charge density distribution of MnSe bilayers with AB and BA stacking patterns. The yellow (or blue) bubbles denote the accumulation (or depletion) of one spin channel. The blue arrows indicate the direction of electric polarization, while the electrically-controlled in-plane magnetization is schematically represented by the red arrows. **c** Spin-resolved electronic band structures of MnSe bilayer with AB, IS and BA stacking patterns. The color scale indicates the magnitude of in-plane spin $S_{x,y}$ obtained by involving SOC.

as shown in Supplementary Fig. 6. To understand the underlying mechanism of the interfacial AFM coupling, we evaluate the exchange interactions of AB stacking MnSe bilayer using MFT, as listed in Supplementary Table 2. It is found that the interlayer exchange interaction is mainly contributed by J_1 (−1.9 meV) and J_2 (−0.8 meV), as shown in Fig. 3a, whereas other contributions are negligible (<0.1 meV). The intralayer AFM coupling is barely affected in MnSe bilayer compared with MnSe monolayer. The interfacial AFM coupling in MnSe bilayer originates from the competition between J_1 and J_2, in which J_2 prevails because of the three equivalent coordination of Mn_2 and Mn_3. The orbital-resolved exchange parameters listed in Supplementary Table 3 show that J_1 and J_2 stem mainly from the a_1-a_1 and a_1-e' hopping, respectively, as depicted in in Fig. 3b. Remarkably, both the a_1-a_1 and a_1-e' hopping are related to the d_{z^2}-p_z-d_{z^2} and d_{z^2}-p_z-d_{yz} (d_{xz}) hybridization, suggesting that the strong hybridization between the p_z orbitals of interfacial Se and the d orbitals of Mn dominates the AFM coupling, as shown in Fig. 3c.

It has been revealed that electric polarization can induce magnetization in an AFM semiconductor via a magnetoelectric effect, which leads to a Zeeman spin splitting in the electronic band structures[40,41]. A linear magnetoelectric coupling has been demonstrated experimentally in an A-type interlayer AFM CrI_3

bilayer[41]. Via symmetry analysis, 21 centrosymmetric magnetic point groups (MPGs) were identified to accommodate electrically controllable Zeeman spin splitting where the electric field acts as an internal effective magnetic field[42]. Notably, the MPG of the MnSe monolayer with an isotropic in-plane Neel-type AFM configuration (2'/m) is one of the 21 MPGs, implying the feasibility of electrically controllable Zeeman spin splitting.

Remarkably, as shown in Fig. 2c, the interlayer inequivalence between two MnSe monolayers of a MnSe bilayer leads to electron redistribution and thus out-of-plane electric polarization. Zeeman spin splitting can therefore occur in the MnSe bilayer, which lifts the degeneracy of the two spin channels in the electronic band structure of the ferroelectric MnSe bilayer. The Zeeman spin splitting at the Γ and K points are 75 and 300 meV, which are much larger than those of Fe_2TeO_6 (~55 meV) and $SrFe_2S_2O$ (~30 meV) under an external electric field of 6 MW cm^{-1}[42]. The electron redistribution in the spin-polarized bands according to the Fermi-Dirac distribution function generates nonzero net magnetic moment which are dependent on the strength of intrinsic out-of-plane built-in electric field, as shown in Fig. 4a. The electron redistribution due to the Zeeman spin splitting is depicted in Fig. 4b. For the AB stacking pattern, the electrons in the spin-down channel transfer from the upper Mn
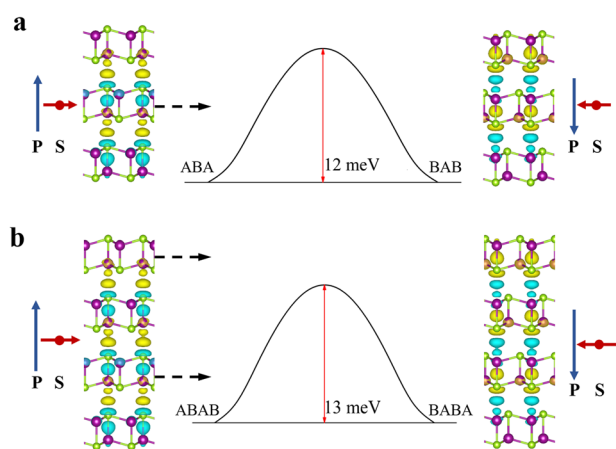
Fig. 5 Sliding ferroelectricity and magnetoelectric coupling in MnSe multilayer. a and **b** Ferroelectric switching pathway of MnSe trilayer and tetralayer, in which the ferroelectric switching barrier are marked by red double-sided arrows. The directions of electric polarization (P) and electron spin (S) are indicated by blue and red arrows, respectively.

atoms to the lower Se atoms at the interface, resulting in net magnetic moments of 8 mμ_B per unit cell. For the BA stacking pattern, the spin-up electrons transfer from lower Mn atom to upper Se atom at the interface, leading to the opposite net magnetic moment of 8 mμ_B per unit cell. Therefore, accompanied by the inversion of the electric polarization direction via interlayer sliding, the spatial distribution and sign of the net magnetic moment can also be switched, displaying the magnetoelectric coupling characteristics, as illustrated in Fig. 4a. The MAE calculations involving SOC show that MnSe bilayer still favors isotropic in-plane magnetization rather than out-of-plane magnetization, as shown in Supplementary Fig. 7, similar to MnSe monolayer. In the magnetoelectric effect, the electric field induces magnetization $M_\beta \propto P_\alpha$ ($\alpha, \beta = x, y, z$), yielding a Zeeman-like Hamiltonian $\chi_{\alpha\beta} P_\alpha \sigma_\beta$ where the tensor $\chi_{\alpha\beta}$ describes the coupling between electric polarization (P_α) and electronic spinσ_β (σ_β represents Pauli matrix)[40]. Therefore, the direction of the in-plane magnetization in the MnSe bilayer can be switched by reversing the electric polarization (i.e., internal effective magnetic field $B_\beta^{eff} \propto \chi_{\alpha\beta} P_\alpha$) via interlayer sliding, as shown in Fig. 4b. This is also consistent with the variation of the electronic band structures of the two stacking patterns, as shown in Fig. 4c. The degeneracy of the two spin channels is lifted oppositely in the AB and BA stacking patterns, and the Zeeman spin splitting is more remarkable near the K point, which can be attributed to the strong interlayer hybridization between Mn-d_{z^2} and Se-p_z orbitals. For the IS which is centrosymmetric, electric polarization and spin-polarization disappear simultaneously, verifying the characteristics of magnetoelectric coupling. We also adopt the D3 and D3(BJ) methods of Grimme to describe the vdW interaction in MnSe bilayer. Our calculations show that the electric polarization, the moderate sliding energy barrier and the magnetoelectric coupling are well preserved in MnSe bilayer, as shown in Supplementary Fig. 9, suggesting that they are independent of the vdW functional employed in the DFT calculations.

The electric polarization and magnetoelectric coupling can be improved in MnSe trilayer and tetralayer, as shown in Fig. 5a, b. For the MnSe trilayer, we consider two energetically degenerate stacking patterns (ABA and BAB) with opposite electric polarization which are switchable via lateral sliding of the middle monolayer relative to the top and bottom monolayers. For MnSe tetralayer, the two switchable ferroelectric states have the stacking patterns of ABAB and BABA where the out-of-plane electric polarization can be reversed by the lateral sliding of the second

and fourth monolayers. As shown in Supplementary Fig. 10, the electric polarization of the MnSe trilayer and tetralayer are respectively 6.7 and 10.6 pC m^{-1}, which are larger than those of the MnSe bilayer. Importantly, all the interlayer magnetic interactions of MnSe multilayer favor interfacial AFM coupling, as reported in Supplementary Table 4, which originate from the same underlying mechanism of MnSe bilayer. Therefore, the net magnetic moments are improved to 16 mμ_B (trilayer) and 24 mμ_B (tetralayer) per unit cell, which are exactly twice and three times compared with MnSe bilayer, respectively, showing a linear relation of magnetoelectric coupling as the stacking number. The energy barriers for the lateral sliding are 12 (trilayer) and 13 (tetralayer) meV per formula, respectively, which still lower than or comparable to most 2D ferroelectric material like In_2Se_3 (~ 60 meV per formula)[39], indicating the feasibility of vertical integration for nanoelectronics device.

Magnetoelectric coupling tuned by external strain and/or hole doping

The flexibility of 2D vdW materials enable significant response of electronic band structures to the external strain[43]. We therefore investigate the electric polarization and magnetoelectric coupling of MnSe bilayer under the compressive strain along the out-of-plane direction and the biaxial in-plane tensile strain. The compressive strain along the out-of-plane direction can be quantized as the variation of the interlayer distance between top and bottom Se atom (d) relative to the equilibrium state (d_0), denoted as $\sigma_z = (d_0 - d)/d_0$. With the increase of compressive strain (decrease of interlayer distance), the interlayer coupling between the two monolayers is enhanced, which improves the electric polarization and net magnetic moment, as shown in Fig. 6a. At $\sigma_z = 0.1$, the electric potential difference between the two monolayers is improved to 0.39 eV and the net magnetic moment become 19 mμ_B per unit cell, which are about two times than those of the equilibrium state. This is accordance with the evolution of the electronic band structures. With the increase of compressive strain, the Zeeman spin splitting of the electronic band increases, as shown in Supplementary Fig. 11a, which can be ascribed to the direct enhancement of hybridization of Mn d and Se p_z orbitals at the interface of MnSe bilayer along the out-of-plane direction.

The in-plane biaxial strain is defined as $\sigma_{x/y} = (a - a_0)/a_0$, where a and a_0 are the lattice constants of the strain and equilibrium states. With the increase of $\sigma_{x/y}$ (negative for compressive strain and positive for tensile strain), the electric polarization and magnetic moment are improved, as shown in Fig. 6b. The compressive strain along the in-plane direction suppresses the electric polarization and the magnetoelectric coupling. In particular, the polarization and magnetic moment almost vanish when the compressive strain attains $\sigma_{x/y} = 0.1$. The in-plane tensile strain, however, enhances the electric polarization and magnetic moment. Moreover, the response of the electronic band structures to the tensile strain is quite remarkable, as shown in Supplementary Fig. 11b. The highest valence bands energy in the region near the K point increases with the increase of tensile, and the lowest conductance band energy at the Γ point is reduced rapidly, making the strained MnSe bilayer be a direct-band-gap semiconductor as $\sigma_{x/y}$ ranging from 0.02 to 0.06.

Electron or hole doping is also available for regulating the electric and magnetic properties of semiconductors. Considering the spin polarized valence band relevant to local net magnetic moment of Se atoms, we therefore calculate the variation of the induced itinerant magnetic moment of the MnSe bilayer in response to hole doping. For the AB stacking pattern, with the increase of hole doping concentration, the magnetism moments start to reach the negative maximum, then becomes positive rapidly, and reach the positive maximum (~ 0.3 μ_B per unit cell) at
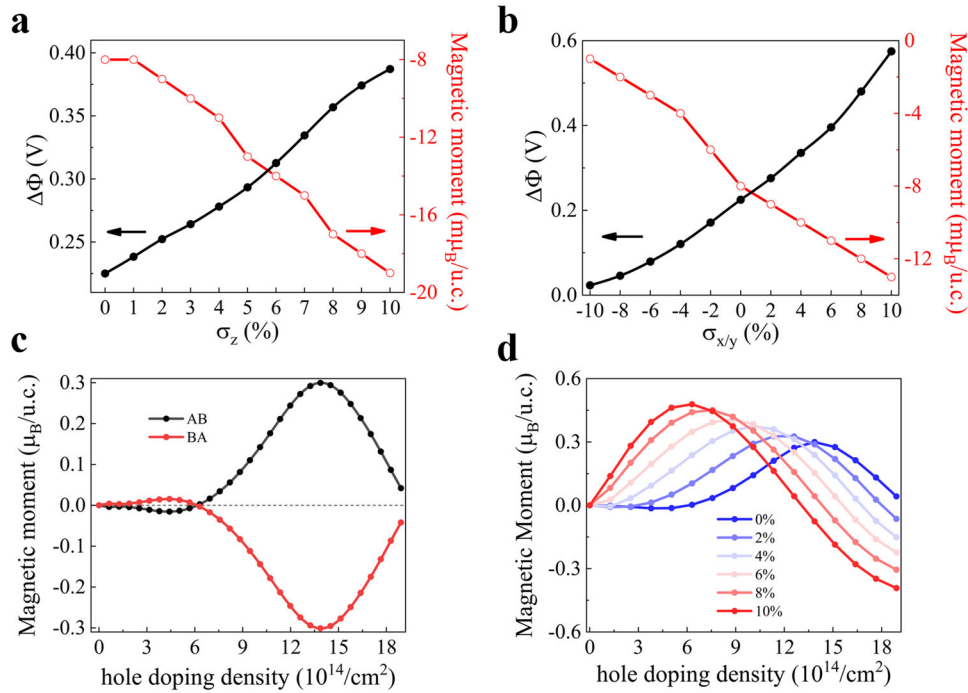
Fig. 6 Tunability of ferroelectricity and magnetoelectric coupling in MnSe bilayer. Variation of electric potential difference and net magnetic moments of AB-stacked MnSe bilayer as a function of **a** out-of-plane pressure and **b** biaxial in-plane strain. Hole doping dependence of net magnetic moment for **c** AB and BA-stacked MnSe bilayer and **d** AB-stacked MnSe bilayer under different biaxial tensile strain.

the hole doping concentration of 1.39×10^{15} cm^{-2}, as shown in Fig. 6c and Supplementary Fig. 12a. The MnSe bilayer with BA stacking pattern, the variation of magnetic moment shows an opposite trend. This implies that the sign of the improved magnetic moments in the hole-doped MnSe bilayer can also be switched via lateral sliding between the two monolayers. Additionally, as shown in Supplementary Fig. 11b, the highest valence bands energy in the region near the K point remarkably increases with the increase of in-plane biaxial tensile strain, while the large Zeeman spin splitting is preserved. We therefore consider the synergistic effect of in-plane tensile strain and hole doping on the magnetization of MnSe bilayer. Our calculations reveal that maximal magnetic moments in the hole-doped MnSe bilayer under in-plane biaxial tensile are further improved and the corresponding hole-doping concentration is reduced compared with the unstrained MnSe bilayer, as shown in Fig. 6d. Under the biaxial tensile strain of $\sigma_{x/y} = 0.1$, the expected hole-doping concentration is decreased to 6.3×10^{14} cm^{-2}, which is attainable in experiment[44–46], as shown in Supplementary Fig. 12b. This offers a promising approach for enhancing the magnetoelectric coupling effect of the MnSe bilayer. More interestingly, the stacking-dependent multiferroicity of the MnSe bilayer enables tunable electric polarization and magnetic moiré patterns by forming twisted MnSe bilayer, which is expected to open an avenue for study of 2D multiferroicity.

DISCUSSION

In summary, we demonstrate from first-principles calculations MnSe multilayers have SFE along with magnetoelectric effect in which both the directions of electric polarization and magnet moment can be switched via lateral interlayer sliding. The electric polarization of MnSe bilayer is stronger than that of BN bilayer and can be further improved in MnSe trilayer and tetralayer. Moreover, the electric polarization and the corresponding magnetism can be enhanced by applying moderate out-of-plane compressive strain

or biaxial in-plane tensile strain and/or hole doping. The moderate sliding energy barrier, switchable electric polarization and magnetism suggest the promising potential of MnSe in multiferroic and spintronic applications.

METHODS

Our first-principles calculations within the density functional theory (DFT) are carried out using the Vienna Ab Initio Simulation Package (VASP) code[47,48]. The generalized gradient approximation in the Perdew–Burke–Ernzerhof (GGA-PBE) is adopted for the exchange-correlation functional[49] and the projector-augmented wave (PAW) pseudopotentials method[50] are applied to describe the interaction between the ions and valence electrons. The electron wavefunctions are expanded by a plane-wave basis with the kinetic energy cutoff of 500 eV. The DFT-D2, D3 and D3(BJ) methods of Grimme[51–53] are included to describe the van der Waals interaction. A large vacuum space up to 20 Å is set in the out-of-plane direction to avoid spurious interaction between images. The Brillouin zone (BZ) is sampled with Γ-centered $9 \times 9 \times 1$ and $13 \times 13 \times 1$ Monkhorst-Pack k mesh[54] for geometry optimization and electronic structure self-consistent calculations, respectively. The geometry structure is fully relaxed until the force on each atom is less than 0.01 eV Å^{-1}, and the electronic structure self-consistent convergence criteria is set to 10^{-7} eV. The GGA + U approach[55] with $U_{eff} = 2.3$ eV for 3d electron of Mn atom is used to treat on-site Coulomb interaction, which is reasonably validated in previous report[36]. The climbing image nudged elastic band (CINEB) method[56] is used to estimate the ferroelectric switching energy barrier, and the Berry phase approach[57,58] is applied to evaluate the electric polarization. The interatomic magnetic interactions are obtained by Green's function method based on magnetic force theory (MFT) performed by TB2J code[59], in which the Maximally localized Wannier functions (MLWFs) are calculated by Wannier90[60] interfaced with the VASP code.

DATA AVAILABILITY

CODE AVAILABILITY

REFERENCES

1. Scott, J. F. Applications of modern ferroelectrics. *Science* **315**, 954–959 (2007).
2. Ghosez, P. & Rabe, K. M. Microscopic model of ferroelectricity in stress-free $PbTiO_3$ ultrathin films. *Appl. Phys. Lett.* **76**, 2767–2769 (2000).
3. Tenne, D. A. et al. Ferroelectricity in ultrathin $BaTiO_3$ films: probing the size effect by ultraviolet Raman spectroscopy. *Phys. Rev. Lett.* **103**, 177601 (2009).
4. Ravindran, P., Vidya, R., Kjekshus, A., Fjellvag, H. & Eriksson, O. Theoretical investigation of magnetoelectric behavior in $BiFeO_3$. *Phys. Rev. B* **74**, 224412 (2006).
5. Seidel, J. et al. Conduction at domain walls in oxide multiferroics. *Nat. Mater.* **8**, 229–234 (2009).
6. Junquera, J. & Ghosez, P. Critical thickness for ferroelectricity in perovskite ultrathin films. *Nature* **422**, 506–509 (2003).
7. Duan, C. G., Sabirianov, R. F., Mei, W. N., Jaswal, S. S. & Tsymbal, E. Y. Interface effect on ferroelectricity at the nanoscale. *Nano Lett.* **6**, 483–487 (2006).
8. Chang, K. et al. Discovery of robust in-plane ferroelectricity in atomic-thick SnTe. *Science* **353**, 274–278 (2016).
9. Chang, K. et al. Microscopic manipulation of ferroelectric domains in SnSe monolayers at room temperature. *Nano Lett.* **20**, 6590–6597 (2020).
10. Higashitarumizu, N. et al. Purely in-plane ferroelectricity in monolayer SnS at room temperature. *Nat. Commun.* **11**, 2428 (2020).
11. Belianinov, A. et al. $CuInP_2S_6$ room temperature layered ferroelectric. *Nano Lett.* **15**, 3808–3814 (2015).
12. Liu, F. C. et al. Room-temperature ferroelectricity in $CuInP_2S_6$ ultrathin flakes. *Nat. Commun.* **7**, 12357 (2016).
13. Zhou, Y. et al. Out-of-plane piezoelectricity and ferroelectricity in layered alpha-In_2Se_3 nanoflakes. *Nano Lett.* **17**, 5508–5513 (2017).
14. Zheng, C. X. et al. Room temperature in-plane ferroelectricity in van der Waals In_2Se_3. *Sci. Adv.* **4**, eaar7720 (2018).
15. Fei, Z. Y. et al. Ferroelectric switching of a two-dimensional metal. *Nature* **560**, 336–339 (2018).
16. Stern, M. V. et al. Interfacial ferroelectricity by van der Waals sliding. *Science* **372**, 1462–1466 (2021).
17. Woods, C. R. et al. Charge-polarized interfacial superlattices in marginally twisted hexagonal boron nitride. *Nat. Commun.* **12**, 347 (2021).
18. Yasuda, K., Wang, X. R., Watanabe, K., Taniguchi, T. & Jarillo-Herrero, P. Stacking-engineered ferroelectricity in bilayer boron nitride. *Science* **372**, 1458–1462 (2021).
19. Sharma, P. et al. A room-temperature ferroelectric semimetal. *Sci. Adv.* **5**, eaax5080 (2019).
20. Xiao, J. et al. Berry curvature memory through electrically driven stacking transitions. *Nat. Phys.* **16**, 1028–1034 (2020).
21. Weston, A. et al. Interfacial ferroelectricity in marginally twisted 2D semiconductors. *Nat. Nanotechnol.* **17**, 390–395 (2022).
22. Wang, X. et al. Interfacial ferroelectricity in rhombohedral-stacked bilayer transition metal dichalcogenides. *Nat. Nanotechnol.* **17**, 367–371 (2022).
23. Wan, Y. et al. Room-temperature ferroelectricity in 1T´-ReS_2 multilayers. *Phys. Rev. Lett.* **128**, 067601 (2022).
24. Rogee, L. et al. Ferroelectricity in untwisted heterobilayers of transition metal dichalcogenides. *Science* **376**, 973–978 (2022).
25. Li, L. & Wu, M. H. Binary compound bilayer and multilayer with vertical polarizations: two-dimensional ferroelectrics, multiferroics, and nanogenerators. *ACS Nano* **11**, 6382–6388 (2017).
26. Yang, Q., Wu, M. H. & Li, J. Origin of two-dimensional vertical ferroelectricity in WTe_2 bilayer and multilayer. *J. Phys. Chem. Lett.* **9**, 7160–7164 (2018).
27. Wang, H. & Qian, X. Ferroelectric nonlinear anomalous Hall effect in few-layer WTe_2. *npj Comput. Mater.* **5**, 119 (2019).
28. Gao, Y. Y., Gao, M. Y. & Lu, Y. R. Two-dimensional multiferroics. *Nanoscale* **13**, 19324–19340 (2021).
29. Eerenstein, W., Mathur, N. D. & Scott, J. F. Multiferroic and magnetoelectric materials. *Nature* **442**, 759–765 (2006).
30. Fiebig, M., Lottermoser, T., Meier, D. & Trassin, M. The evolution of multiferroics. *Nat. Rev. Mater.* **1**, 16046 (2016).
31. Dong, S., Xiang, H. & Dagotto, E. Magnetoelectricity in multiferroics: a theoretical perspective. *Natl Sci. Rev.* **6**, 629–641 (2019).
32. Dong, S., Liu, J. M., Cheong, S. W. & Ren, Z. F. Multiferroic materials and magnetoelectric physics: symmetry, entanglement, excitation, and topology. *Adv. Phys.* **64**, 519–626 (2015).
33. Lu, C. L., Wu, M., Lin, L. & Liu, J. M. Single-phase multiferroics: new materials, phenomena, and physics. *Natl Sci. Rev.* **6**, 653–668 (2019).
34. Liu, X., Pyatakov, A. P. & Ren, W. Magnetoelectric coupling in multiferroic bilayer VS_2. *Phys. Rev. Lett.* **125**, 247601 (2020).
35. Yan, H. et al. Electric-field-controlled antiferromagnetic spintronic devices. *Adv. Mater.* **32**, 1905603 (2020).
36. Aapro, M. et al. Synthesis and properties of monolayer mnse with unusual atomic structure and antiferromagnetic ordering. *ACS Nano* **15**, 13794–13802 (2021).
37. Sattar, S., Islam, M. F. & Canali, C. M. Monolayer MnX and Janus XMnY (X, Y = S, Se, Te): a family of two-dimensional antiferromagnetic semiconductors. *Phys. Rev. B* **106**, 085410 (2022).
38. Lin, Z. Z., Si, C., Duan, S. R., Wang, C. & Duan, W. H. Rashba splitting in bilayer transition metal dichalcogenides controlled by electronic ferroelectricity. *Phys. Rev. B* **100**, 155408 (2019).
39. Ding, W. J. et al. Prediction of intrinsic two-dimensional ferroelectrics in In_2Se_3 and other III_2-VI_3 van der Waals materials. *Nat. Commun.* **8**, 14956 (2017).
40. Fiebig, M. Revival of the magnetoelectric effect. *J. Phys. D: Appl. Phys.* **38**, R123–R152 (2005).
41. Jiang, S., Shan, J. & Mak, K. F. Electric-field switching of two-dimensional van der Waals magnets. *Nat. Mater.* **17**, 406 (2018).
42. Zhao, H. J. et al. Zeeman effect in centrosymmetric antiferromagnetic semiconductors controled by an electric field. *Phys. Rev. Lett.* **129**, 187602 (2022).
43. Miao, F., Liang, S. J. & Cheng, B. Straintronics with van der Waals materials. *npj Quantum Mater.* **6**, 59 (2021).
44. Efetov, D. K. & Kim, P. Controlling electron-phonon interactions in graphene at ultrahigh carrier densities. *Phys. Rev. Lett.* **105**, 256805 (2010).
45. Ye, J. T. et al. Accessing the transport properties of graphene and its multilayers at high carrier density. *Proc. Natl Acad. Sci. USA* **108**, 13002–13006 (2011).
46. Li, L. J. et al. Controlling many-body states by the electric-field effect in a two-dimensional material. *Nature* **529**, 185–189 (2016).
47. Kresse, G. & Hafner, J. AB initio molecular dynamics for open-shell transition metals. *Phys. Rev. B* **48**, 13115 (1993).
48. Kresse, G. & Furthmuller, J. Efficiency of ab-initio total energy calculations for metals and semiconductors using a plane-wave basis set. *Comp. Mater. Sci.* **6**, 15–50 (1996).
49. Perdew, J. P., Burke, K. & Ernzerhof, M. Generalized gradient approximation made simple. *Phys. Rev. Lett.* **77**, 3865 (1996).
50. Kresse, G. & Joubert, D. From ultrasoft pseudopotentials to the projector augmented-wave method. *Phys. Rev. B* **59**, 1758 (1999).
51. Grimme, S. Semiempirical GGA-type density functional constructed with a long-range dispersion correction. *J. Comput. Chem.* **27**, 1787–1799 (2006).
52. Grimme, S., Antony, J., Ehrlich, S. & Krieg, H. A consistent and accurate ab initio parameterization of density functional dispersion correction (DFT-D) for the 94 elements H-Pu. *J. Chem. Phys.* **132**, 154104 (2010).
53. Grimme, S., Ehrlich, S. & Goerigk, L. Effect of the damping function in dispersion corrected density functional theory. *J. Comput. Chem.* **32**, 1456–1465 (2011).
54. Monkhorst, H. J. & Pack, J. D. Special points for Brillouin-zone integrations. *Phys. Rev. B* **13**, 5188 (1976).
55. Dudarev, S. L., Botton, G. A., Savrasov, S. Y., Humphreys, C. J. & Sutton, A. P. Electron-energy-loss spectra and the structural stability of nickel oxide: An LSDA +U study. *Phys. Rev. B* **57**, 1505 (1998).
56. Henkelman, G., Uberuaga, B. P. & Jonsson, H. A climbing image nudged elastic band method for finding saddle points and minimum energy paths. *J. Chem. Phys.* **113**, 9901–9904 (2000).
57. Kingsmith, R. D. & Vanderbilt, D. Theory of polarization of crystalline solids. *Phys. Rev. B* **47**, 1651(R) (1993).
58. Resta, R. Macroscopic polarization in crystalline dielectrics: the geometric phase approach. *Rev. Mod. Phys.* **66**, 899 (1994).
59. He, X., Helbig, N., Verstraete, M. J. & Bousquet, E. TB2J: A python package for computing magnetic interaction parameters. *Comput. Phys. Commun.* **264**, 107938 (2021).
60. Mostofi, A. A. et al. wannier90: a tool for obtaining maximally-localized Wannier functions. *Comput. Phys. Commun.* **178**, 685 (2008).

AUTHOR CONTRIBUTIONS

M.Z. conceived the project. K.L. and X.M. performed the first-principles calculations and conducted theoretical analysis. S.X. and Y.L. conducted the theoretical analysis. K.L. and M.Z. wrote the manuscript.

COMPETING INTERESTS

The authors declare no competing interests.

ADDITIONAL INFORMATION

Supplementary information The online version contains supplementary material available at https://doi.org/10.1038/s41524-023-00972-2.

Correspondence and requests for materials should be addressed to Mingwen Zhao.

Reprints and permission information is available at http://www.nature.com/reprints

Publisher's note Springer Nature remains neutral with regard to jurisdictional claims in published maps and institutional affiliations.